Recovery from population III supernova explosions and the onset of second generation star formation

Myoungwon Jeon[1]⋆, Andreas H. Pawlik[2], Volker Bromm[1], and Miloš Milosavljević[1]

[1]*Department of Astronomy, University of Texas, Austin, TX 78712, USA*
[2]*Max-Planck-Institut für Astrophysik, Karl-Schwarzschild-Strasse 1, 85748 Garching bei München, Germany*

ABSTRACT

We use cosmological simulations to assess how the explosion of the first stars in supernovae (SNe) influences early cosmic history. Specifically, we investigate the impact by SNe on the host systems for Population III (Pop III) star formation and explore its dependence on halo environment and Pop III progenitor mass. We then trace the evolution of the enriched gas until conditions are met to trigger second-generation star formation. To this extent, we quantify the recovery timescale, which measures the time delay between a Pop III SN explosion and the appearance of cold, dense gas, out of which second-generation stars can form. We find that this timescale is highly sensitive to the Pop III progenitor mass, and less so to the halo environment. For Pop III progenitor masses $M_* \lesssim 40\,M_\odot$, recovery is prompt, ~ 10 Myr. For more massive progenitors, including those exploding in pair instability SNe, second-generation star formation is delayed significantly, for up to a Hubble time. The dependence of the recovery time on the mass of the SN progenitor is mainly due to the ionizing impact of the progenitor star. Photoionization heating increases the gas pressure and initiates a hydrodynamical response that reduces the central gas density, an effect that is stronger in more massive and hence more luminous progenitors. The gas around lower mass Pop III stars remains therefore denser and hence the SN remnants cool more rapidly, facilitating the subsequent re-condensation of the gas and formation of a second generation of stars. In most cases, the second-generation stars are already metal-enriched, thus belonging to Population II. The recovery timescale is a key quantity governing the nature of the first galaxies, able to host low-mass, long-lived stellar systems. These in turn are the target of future deep-field campaigns with the *James Webb Space Telescope*.

Key words: cosmology: theory – galaxies: formation – galaxies: high-redshift – HII regions – hydrodynamics – intergalactic medium – supernovae: physics.

1 INTRODUCTION

One of the most intriguing aspects of modern cosmology is the formation of the first stars and galaxies. The first stars, so-called Population III (Pop III), were responsible for the transition of the Universe from its simple, metal-free state to one of ever increasing complexity. Therefore, exploring their feedback on the pristine intergalactic medium (IGM) has been one of the key themes in elucidating early cosmic evolution (e.g., Loeb & Furlanetto 2013; Wiklind et al. 2013). Pop III stars started forming at redshifts as early as $z \gtrsim 30$ out of primordial gas in dark matter (DM) minihaloes of total mass $M \sim 10^5 - 10^6\,M_\odot$ (e.g. Haiman et al. 1996; Tegmark et al. 1997; Bromm et al. 2002; Yoshida et al. 2003). Once the first stars began emitting ionizing radiation, the gas inside minihalo hosts was photoheated to a few 10^4 K. As a consequence, pressure-driven outflows significantly suppressed central gas densities. After their brief lifetime of $\sim 10^6 - 10^7$ yr, Pop III stars may

have exploded as supernovae (SNe) or collapsed directly in black holes (BHs), possibly without explosion. The subsequent evolution of the surrounding IGM was shaped by the feedback from such Pop III remnants (e.g. Barkana & Loeb 2001; Bromm & Larson 2004; Ciardi & Ferrara 2005; Bromm et al. 2009).

If a Pop III star died in a SN explosion, the ambient gas, already rarified by the radiation-hydrodynamical reaction to the star's ionizing radiation, was shock heated and hydrodynamically evacuated from the minihalo as the shock traversed the halo. The dispersal of heavy elements and dust from the first SNe initiated the long history of cosmic chemical enrichment (e.g. Karlsson et al. 2013). This enrichment was critical for star formation because the metal-enriched dusty gas was able to cool to the temperature floor set by the cosmic microwave background, $T_{\rm CMB} = 2.7\,{\rm K}\,(1 + z)$, similar to the characteristic temperatures of star-forming clouds in the nearby Universe. Such low temperatures were hard to reach in metal-free primordial gas, in which molecular hydrogen was the main available coolant. Therefore, the initial stellar mass function (IMF) is expected to have changed from the top-heavy IMF,

⋆ E-mail: myjeon@astro.as.utexas.edu

predicted for Pop III, to the low-mass dominated IMF of Population II (Pop II), once enrichment levels exceeded a critical threshold. Whether this threshold was linked to fine-structure line cooling or dust-continuum cooling is still debated, but there is general agreement that such a 'critical metallicity' played an important role (e.g. Omukai 2000; Bromm et al. 2001; Schneider et al. 2002; Bromm & Loeb 2003; Ji et al. 2014). If, on the other hand, a Pop III star ended its life as a BH via direct collapse, subsequent gas accretion onto the remnant may have resulted in a miniquasar—a stellar mass black hole accreting near the Eddington limit —that emitted X-rays (e.g., Glover & Brand 2003; Kuhlen & Madau 2005; Milosavljević et al. 009a,b; Alvarez et al. 2009; Park & Ricotti 2011; Venkatesan & Benson 2011; Wheeler & Johnson 2011; Jeon et al. 2012, 2014).

The fate of a Pop III star was determined by its mass and degree of rotation. Non-rotating Pop III stars with masses between $10\,M_\odot$ and $40\,M_\odot$ are thought to end their lives as core collapse SNe, or as highly energetic pair-instability supernovae (PISNe) for masses in the range of $140\,M_\odot \lesssim M_* \lesssim 260\,M_\odot$ (Heger & Woosley 2002), or directly collapse into a BH for other progenitor masses (Heger et al. 2003). Stellar rotation may introduce significant changes to this picture (Maeder & Meynet 2012). Core-collapse of rapidly rotating stars may trigger energetic hypernovae (e.g. Umeda & Nomoto 2005), and the lower mass-limit for a PISN could be reduced to $\sim 85\,M_\odot$ (Chatzopoulos & Wheeler 2012; Yoon et al. 2012).

The characteristic mass scale of Pop III stars remains an open question (e.g. Bromm 2013). Previously, the first stars were thought to be isolated and rather massive, with a characteristic mass of $\sim 100\,M_\odot$ (e.g., Abel et al. 2002; Bromm et al. 2002; Yoshida et al. 2006). However, recent improved simulations have identified a ubiquitous disk fragmentation mode, revising the typical mass scale downwards to a few $10\,M_\odot$ (Turk et al. 2009; Stacy et al. 2010; Clark et al. 2011; Prieto et al. 2011; Smith et al. 2011; Greif et al. 2011, 2012; Stacy & Bromm 2013; Dopcke et al. 2013). Moreover, radiative feedback has recently been shown to put an additional limit to the masses of these stars (e.g., Hosokawa et al. 2011; Stacy, Greif, & Bromm 2012; Hirano et al. 2014). Consequently, Pop III stars were more likely to end their lives as core collapse SNe, rather than PISNe. In addition, observed abundance patterns in the atmospheres of metal-poor Galactic halo stars, expected to form out of gas enriched by Pop III stars, have so far not exhibited the strong elemental odd-even effect and the absence of any neutron-capture elements, which would be manifest signatures for PISNe. Pop III stellar masses may have thus been limited to $\lesssim 140\,M_\odot$ (Tumlinson 2006; Heger & Woosley 2010; Joggerst et al. 2010; Keller et al. 2014).

There has been a number of numerical studies investigating the impact of early SNe on the gas surrounding the explosion sites and on the assembly process of the first galaxies (Bromm et al. 2003; Kitayama & Yoshida 2005; Greif et al. 2007, 2010; Whalen et al. 2008; Wise & Abel 2008; Maio et al. 2010; Bland-Hawthorn et al. 2011; Ritter et al. 2012; Wise et al. 2012). Since the first stars were initially estimated to have very large masses $M_* \gtrsim 100\,M_\odot$, most of these early studies focused on the impact of the more energetic PISNe. For instance, Greif et al. (2010) and Wise & Abel (2008) followed the impact of a single PISN with an explosion energy of 10^{52} ergs until an atomic-cooling halo assembled at $z \approx 10$. They found that even a single PISN explosion could enrich the region out of which the first galaxies formed to supercritical metallicities $Z > 10^{-3}\,Z_\odot$, such that the first galaxies would typically host already metal-enriched Pop II stellar systems.

In contrast to PISNe, the impact of the less energetic core collapse SNe critically depended on the Pop III progenitor mass and their environments, as was already found in one-dimensional, radiation-hydrodynamic simulations (Kitayama & Yoshida 2005; Whalen et al. 2008). For instance, the gas in minihaloes with masses close to the cooling threshold for collapse, $\sim 10^5 - 10^6\,M_\odot$, was more vulnerable to photoionization heating by the stellar progenitor, which decreased the density of the gas into which the SN exploded. Such conditions allowed SN ejecta to more easily escape the haloes. On the other hand, the ionizing radiation from Pop III stars inside more massive $\sim 10^7\,M_\odot$ host systems remained more strongly confined, such that the SN remnants encounter mostly intact high-density clouds. Most of the SN explosion energy then was rapidly radiated away, and this impeded the escape of the metal-enriched gas to the IGM.

Ritter et al. (2012) investigated such a case of prompt fallback in a three dimensional, cosmological grid-based hydrodynamic simulation, where a $40\,M_\odot$ SN exploded in a minihalo of $\sim 10^6\,M_\odot$. The SN remnant remained partially trapped within the minihalo. Roughly half of the ejecta turned around and fell back toward the center of the halo, with 10% of the ejecta reaching the center in $\sim 10\,$Myr. The average metallicity of the combined returning ejecta and the pristine cosmic web filaments feeding into the halo center was $\sim 0.001 - 0.01\,Z_\odot$, but the two fluids remained unmixed until accreting onto a central hydrostatic core, unresolved in the simulation. Ritter et al. concluded that if Pop III stars had moderate masses, they could promptly enrich the host minihalos with metals and trigger Pop II star formation.

While these pioneering studies brought into focus the key physics, they either considered only a few specific cases, not exploring the dependence on a varying cosmic environment, or employed somewhat simplified initial conditions. Taking into account realistic cosmological initial conditions and exploring a broader parameter space is clearly desirable. As an example, an insufficient number of ionizing photons from $10 - 40\,M_\odot$ Pop III stars to achieve substantial gas evacuation from the host system might produce a highly asymmetric pre-explosion density distribution. The ensuing SN blastwave would then preferentially propagate along low-density channels, usually perpendicular to the cosmic filaments, resulting in highly non-uniform metal dispersal (e.g., Wise & Abel 2008; Greif et al. 2010).

To address the environmental complexity of early SN feedback, we here report on a suite of cosmological radiation-hydrodynamics simulations. We followed the evolution of the SN-processed gas to the point at which the second generation of stars began to form out of this metal-enriched material. We specifically ask: *What is the delay between the initial Pop III star formation event and the re-establishment of conditions for subsequent star formation?* Addressing this question is crucial for understanding the assembly process of the first galaxies and their properties (Bromm & Yoshida 2011).

The severity of the Pop III feedback is reflected in the mass scale of the first galaxies, since stronger feedback requires the assembly of more massive host systems for the SN-processed gas to be able to cool and recondense. This mass scale for the first galaxies in turn determines their luminosities and number density, with important implications for early reionization (for reviews see, e.g., Barkana & Loeb 2001; Barkana 2009; Robertson et al. 2010). Pushing the high redshift frontier by observing the first galaxies is one of the main goals of next-generation facilities, such as the *James Webb Space Telescope* (JWST), the planned extremely large ground-based telescopes, the Atacama Large Millimitre Ar-

Table 1. Properties of host haloes, Pop III progenitors, and SNe.

Halo	$M_{\rm vir}$ [$M_\odot$]	$z_{\rm form}$	M_* [$M_\odot$]	$t_{\rm life}$ [Myr]	$\dot{N}_{\rm ion}$ [s^{-1}]	$E_{\rm SN}$ [ergs]	y	Recovery time [Myr]
HALO1	5×10^5	28	15	10	1.86×10^{48}	1.0×10^{51}	0.05	8.9
HALO1	5×10^5	28	25	6.4	7.58×10^{48}	1.0×10^{51}	0.05	24
HALO1	5×10^5	28	40	3.8	2.47×10^{49}	$0.6, 1.0 \times 10^{51}$	0.05	92, 92
HALO1	5×10^5	28	200	2.2	2.69×10^{50}	10^{52}	0.5	300
HALO2	9×10^5	25	25	6.4	7.58×10^{48}	1.0×10^{51}	0.05	8
HALO2	9×10^5	25	40	3.8	2.47×10^{49}	1.0×10^{51}	0.05	6
HALO3	3×10^5	23	40	3.8	2.47×10^{49}	1.0×10^{51}	0.05	140

From left to right, the columns show the host minihalo identifier, the total virial mass of the minihalo $M_{\rm vir}$, the Pop III star's formation redshift $z_{\rm form}$ and mass M_*, the main-sequence lifetime $t_{\rm life}$, the ionizing photon emission rate $\dot{N}_{\rm ion}$ (Schaerer 2003), the SN energy $E_{\rm SN}$ and metal yield fraction y (Table 2 in Karlsson et al. 2013), and recovery time for return of gas into the center of the host halo (see Section 3). The recovery time for the SN explosion of energy 10^{52} ergs is taken from Greif et al. (2010), who used identical initial conditions.

ray (ALMA), and the Square Kilometre Array (SKA). The observability of the first galaxies will be determined by their star formation efficiencies and stellar IMFs (e.g., Johnson et al. 2009; Pawlik, Milosavljević, & Bromm 2011; Zackrisson et al. 2011).

Recently, it has been suggested that the strength of SN driven outflows may be responsible for the observed dichotomy between carbon-enhanced and carbon-normal metal-poor stars (Cooke & Madau 2014). These authors invoke two classes of SNe with greatly different times for recovery from supernova explosions, such that rapid recovery is connected to weak explosions with large carbon overabundances, and slow recovery with strong explosions with normal carbon yields. Pinning down gas dynamics in the aftermath of Pop III supernovae is clearly essential for completing the picture of how the early Universe evolved and what kind of long-lived relics it left in the nearby Universe.

This paper is organized as follows. Our numerical methodology is described in Section 2 and the simulation results are presented in Section 3. Finally, our main findings are summarized in Section 4. For consistency, all distances are expressed in physical (proper) units unless noted otherwise.

2 NUMERICAL METHODOLOGY

2.1 Gravity, hydrodynamics, and chemistry

We carry out our investigation using the N-body/TreePM Smoothed Particle Hydrodynamics (SPH) code GADGET (Springel 2005; Springel et al. 2001; our specific implementation is based on that discussed in Schaye et al. 2010). Our simulations start with a snapshot from the earlier zoomed simulation of Greif et al. (2010), which was initialized at $z = 99$ in a periodic box of size 1 comoving Mpc. The initial conditions in Greif et al. (2010) were generated by assuming a ΛCDM cosmology with a matter density parameter of $\Omega_{\rm m} = 1 - \Omega_\Lambda = 0.3$, baryon density $\Omega_{\rm b} = 0.04$, present-day Hubble expansion rate $H_0 = 70 \, {\rm km \, s^{-1} Mpc^{-1}}$, spectral index $n_{\rm s} = 1.0$, and normalization $\sigma_8 = 0.9$. We follow the evolution until the gas affected by the radiation of the Pop III progenitor star and the ensuing SN explosion has recollapsed, reaching conditions where a second round of star formation can take place.

Employing nested refinement of the cosmological initial conditions, the masses of dark matter (DM) and SPH gas particles in the highest resolution region with an approximate linear size of 300 comoving kpc are $m_{\rm DM} \approx 33 \, M_\odot$ and $m_{\rm SPH} \approx 5 \, M_\odot$, respectively. Therefore, the baryonic mass resolution is $M_{\rm res} \equiv$
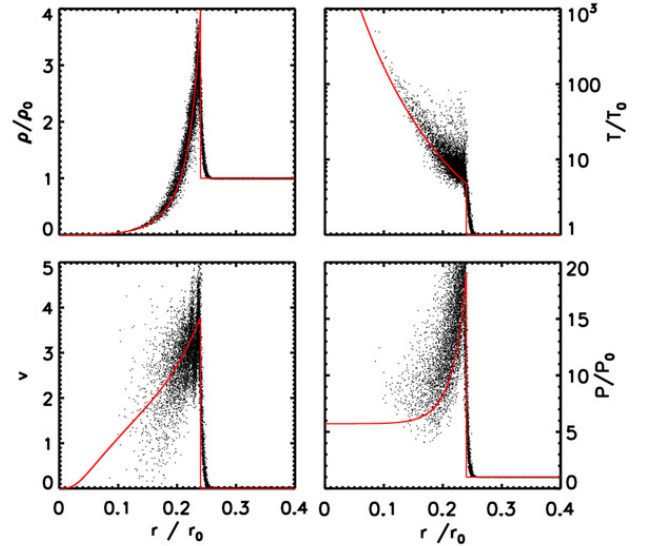

Figure 1. Test of SN blast wave dynamics in the absence of radiative cooling. The shocked gas properties are shown at $t_{\rm sh} = 0.02$ after the SN explosion with $E_0 = 1$. The red solid line is the self-similar Sedov-Taylor solution. The agreement between the simulation and the self-similar solution is reasonable and the location of the shock is captured very well.

$N_{\rm ngb} m_{\rm SPH} \approx 240 \, M_\odot$, where $N_{\rm ngb} = 48$ is the number of particles in the SPH smoothing kernel (Bate & Burkert 1997). This resolution makes it possible to follow the gas evolution to a density of $n_{\rm H} \simeq 10^4 \, {\rm cm^{-3}}$ characteristic of the quasi-hydrostatic loitering state before the onset of the runaway collapse that ultimately leads to Pop III star formation (Abel et al. 2002; Bromm et al. 2002). We adopt a Plummer-equivalent gravitational softening length of 70 comoving pc for both dark matter and baryonic particles.

We use the primordial chemistry and cooling network in Greif et al. (2010), where all relevant cooling mechanisms are taken into account, specifically, H and He collisional ionization, excitation and recombination cooling, bremsstrahlung, inverse Compton cooling, and collisional excitation cooling of H_2 and HD. The code self-consistently solves the non-equilibrium chemistry for 9 species (H, H^+, H^-, H_2, H_2^+, He, He^+, He^{++}, and e^-), as well as for the
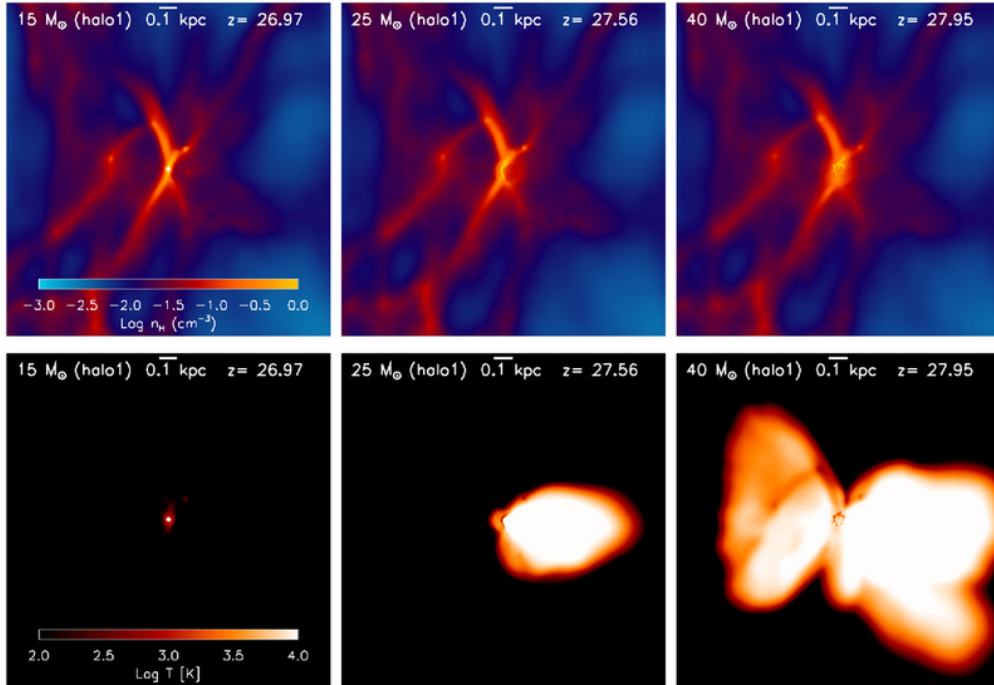
Figure 2. Projected gas density (top) and temperature (bottom) in a slab of size 35 kpc (comoving) and thickness 7 kpc (comoving), centered on the locations of the 15 $M_\odot$, 25 $M_\odot$, and 40 $M_\odot$ Pop III stars (from left to right) in HALO1 at the end of each star's lifetime and just before the subsequent explosion in a SN. The ionizing photons from the stars preferentially propagate into the voids, perpendicular to the high density cosmic filaments, forming noticeable H II regions around the 25 $M_\odot$ and 40 $M_\odot$ stars. The HII region around the 15 $M_\odot$ star is unable to outrun the hydrodynamical shock it generates, leaving it in a highly compact state.

three deuterium species D, D^+, and HD. Moreover, after the SN explodes, the primordial gas is polluted with heavy elements. The code allows us to follow the chemical evolution of C, O, and Si, ejected by the SN explosion, assuming solar relative abundances, and includes the corresponding metal line collisional excitation and cooling rates (Glover & Jappsen 2007). The chemical network comprises the key species, C, C^+, O, O^+, Si, Si^+, and Si^{++}.

2.2 Pop III properties and ionizing radiative transfer

The characteristic mass of the first stars is a matter of intense research. Recent high-resolution simulations have revised the characteristic scale downward to tens of solar masses and have suggested a broad Pop III IMF, as explained in the Introduction. In this work, we aim to explore a representative subset of progenitor masses. We provide the properties of Pop III progenitors and SN explosions in Table 1 (Heger & Woosley 2002; Schaerer 2003; Karlsson et al. 2013). To consider environmental effects on the evolution of Pop III SN remnants, we insert Pop III stars in three different minihaloes inside the most highly resolved region. Properties of these halos are provided in Table 1.

We start our simulations at $z \approx 30$, corresponding to the time just before the first Pop III star has formed. Once the hydrogen number density exceeds $n_{H,max} = 10^4$ cm^{-3}, the highest-density SPH particle is converted into a collisionless sink particle, subsequently accreting neighboring gas particles until its mass has reached the target Pop III progenitor star mass (see Table 1).

The sink particle then becomes a source of ionizing radiation, emitted at a rate averaged over the main sequence lifetime computed by Schaerer (2002). The radiation spectrum is assumed to

be a black-body spectrum at temperature $10^{4.76}$ K, $10^{4.85}$ K, and $10^{4.9}$ K for the stars of 15, 25, and 40 solar mass, respectively (Schaerer 2002). We transport this ionizing radiation using the radiative transfer (RT) code TRAPHIC (Pawlik & Schaye 2008, 2011). TRAPHIC solves the time-dependent RT equation in SPH simulations by tracing photon packets emitted by source particles in a photon-conserving manner. The RT is controlled by a set of parameters, which we choose identical to those employed in Jeon et al. (2014). Recombination radiation is treated in the Case B approximation (for a discussion of the applicability of this approximation see, e.g., Raičević et al. 2014, and references therein).

In addition to the ionizing radiation from Pop III stars, we also track the Lyman-Werner (LW) radiation that dissociates H_2 and HD. The latter is treated in the optical thin limit with a self-shielding correction. For further details on our RT methodology and the treatment of LW radiation we refer the reader to Jeon et al. (2014).

2.3 Supernova energy injection

We explode each SN at the end of the progenitor's main-sequence lifetime. The explosion energy is distributed among the nearest $\bar{N}_{ngb} = 32$ neighbor SPH particles with equal weight. This establishes a strong pressure jump relative to the surrounding medium, in turn launching a blast wave.

Within SPH schemes, particles are often assigned individual time steps, sorted in a hierarchical fashion, such that only a fraction of particles is 'active' at any time. Only the properties of active particles are updated at any given time. Therefore, if a SN blast wave alters the internal energies of neighboring gas particles, only the
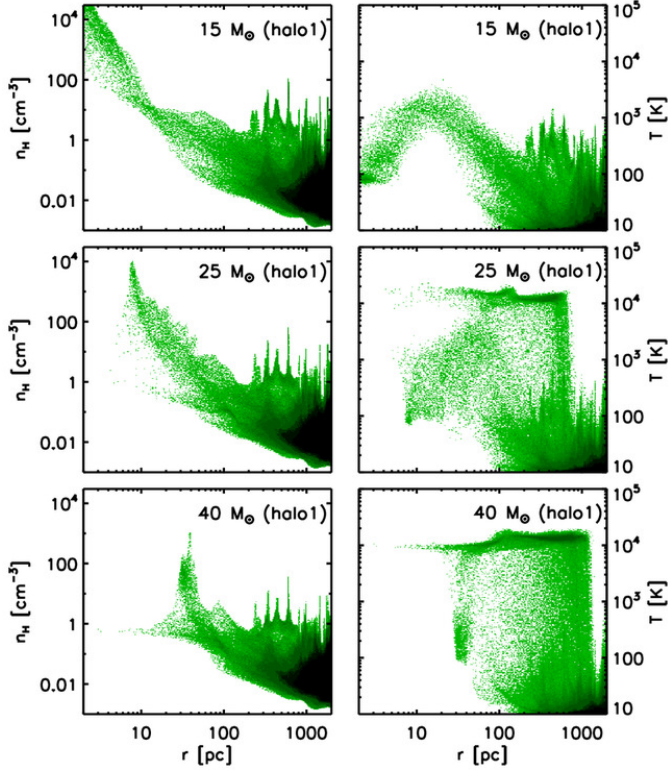
Figure 3. Density (left) and temperature (right) profiles at the end of the progenitor's life, altered by the radiation from the $15\,M_\odot$, $25\,M_\odot$, and $40\,M_\odot$ Pop III stars (from top to bottom) in HALO1. The asymmetric structure of the H II regions around the $25\,M_\odot$ and $40\,M_\odot$ stars, shown in Fig. 2, is reflected in the bifurcation of the gas properties inside $r \lesssim 50$ pc: the gas lying along the cosmic filaments remains dense $n_H \gtrsim 10\,\mathrm{cm}^{-3}$ and cold $T < 10^3$ K, while that in the less dense regions is photoevaporated to $n_H \lesssim 1\,\mathrm{cm}^{-3}$ and photoheated to $T \approx 10^4$ K. The H II region created by the $15\,M_\odot$ star remains too small to significantly impact the distribution of the gas in the halo.

active particles among them are able to react to this sudden change. Inactive particles cannot be updated right away and this introduces serious errors into the hydrodynamics. These errors can be reduced by imposing a sufficiently small upper limit on the individual time steps. However, using such a global constraint on the time steps is computationally expensive.

Instead, in order to elicit a prompt response to energy injection, we employ the time step limiter originally suggested by Saitoh & Makino (2009) and developed further by Durier & Dalla Vecchia (2012). This limiter restricts the time steps of neighboring particles, specifically those within an SPH smoothing kernel, such that the time step ratios do not exceed a given factor f_{step}. However, Durier & Dalla Vecchia (2012) have shown that when only the time step limiter is used, energy conservation may be strongly violated if energy is injected at a random time. To tackle this problem, Durier & Dalla Vecchia (2012) implemented an update scheme where at the time of the SN explosion *all* $\bar{N}_{\mathrm{ngb}}$ neighboring particles inside of the explosion volume become active. In our simulations, we use both the time step limiter and the time step update by adopting the value of $f_{\mathrm{step}} = 4$. This ensures the accurate integration of the SN explosion, and is substantially less computationally expensive than comparably accurate simulations that impose a small global upper limit on the particle time step (e.g., Greif et al. 2007).

We tested our implementation by simulating the self-similar Sedov-Taylor (ST) problem, which has a known analytic solution. Fig. 1 shows the shocked gas properties affected by a SN explosion of energy $E_0 = 1$, at a time $t_{\mathrm{sh}} = 0.02$ after energy injection. Initially, $N = 128^3$ gas particles were uniformly distributed in a glass-like configuration with mean density $\rho_0 = 1$ (White et al. 1996). The initial internal energy was set to $u_0 = 10^{-3}$. We show the self-similar ST solution with red solid lines (e.g., Shu 1992, Durier & Dalla Vecchia 2012). The location of the shock front, $R_{\mathrm{sh}} \sim (E_0 t_{\mathrm{sh}}^2/\rho_0)^{1/5}$, where t_{sh} is the evolution time and ρ_0 the density of the surrounding medium, is consistent with the numerical result. Directly behind the shock, the gas accurately approximates the Rankine-Hugoniot jump conditions for the density, velocity, and pressure, $[\rho_{\mathrm{sh}}, v_{\mathrm{sh}}, P_{\mathrm{sh}}] \equiv [4\rho_0, 3\dot{r}_{\mathrm{sh}}/4, 3\rho_0\dot{r}_{\mathrm{sh}}^2/4] \approx [4, 3.78, 19]$. Here, $\dot{r}_{\mathrm{sh}} \approx 5$ is the shock velocity.

2.4 Metal transport

The modeling of the chemical transport in SPH simulations is a difficult task. In pure SPH schemes, there is no mass flux between particles. Also, for SPH to resolve the turbulent cascade that is the pre-condition for mixing would require much higher resolution than attainable in cosmological simulations. Here, we implement a subgrid prescription for compositional diffusion as in Greif et al. (2009), where metal transport between particles was modelled as a diffusion process (Klessen & Lin 2003). The discretized diffusion equation in the SPH formalism is

$$\frac{dc_i}{dt} = \sum_j K_{ij}(c_i - c_j), \tag{1}$$

with

$$K_{ij} = \frac{m_j}{\rho_i \rho_j} \frac{4D_i D_j}{(D_i + D_j)} \frac{r_{ij} \cdot \nabla_i W_{ij}}{r_{ij}^2}, \tag{2}$$

where c_i is the concentration of SPH particle i, m_i the particle mass, ρ_i the density at the particle location $\mathbf{r}_i$, W_{ij} the smoothing kernel evaluated at $r_{ij} = |\mathbf{r}_i - \mathbf{r}_j|$, the separation between particles i and j, and D_i is a diffusion coefficient associated with particle i.

If a diffusion process is to meaningfully emulate turbulence-assisted chemical mixing, the diffusion coefficient must somehow reflect the amplitude of the local turbulent cascade on subgrid scales. For example, a cascade may be expected in the presence of strong shear that would excite the Kelvin-Helmholtz instability. More generally, one might anticipate the strength of the subgrid turbulent cascade to scale with the amplitude of gas motions on the smallest resolved scales, ignoring the motions on larger scales. In grid-based hydrodynamic simulations, the loss of kinetic energy to subgrid scales has been modeled with a diffusion term with diffusivity $\sim \Delta(\rho K_{\mathrm{sgs}})^{1/2}$, where Δ is the grid spacing and K_{sgs} is the kinetic energy density on subgrid scales (Schmidt et al. 2006; Schmidt & Federrath 2011). In SPH, we replace the grid spacing with the SPH smoothing length $\tilde{l}$ and the kinetic energy density with $\rho \tilde{v}^2$, where $\tilde{v}$ is the velocity dispersion within the SPH kernel, which for particle i equals

$$\tilde{v}_i^2 = \frac{1}{N_{\mathrm{ngb}}} \sum_{j=1}^{N_{\mathrm{ngb}}} |\mathbf{v}_i - \mathbf{v}_j|^2, \tag{3}$$

where $\mathbf{v}_i$ is the velocity of particle i. The diffusion coefficient is then proportional to $\rho \tilde{v} \tilde{l}$ and we adopt
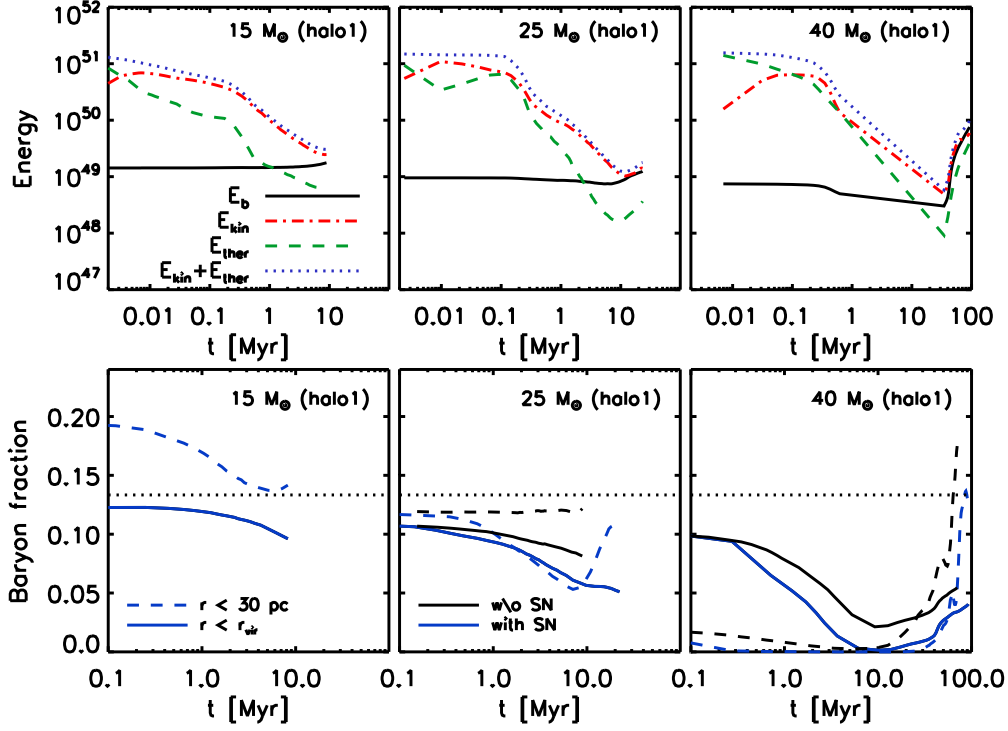
$$D = 2\rho \tilde{v} \tilde{l}. \tag{4}$$

Figure 4. The evolution of the binding (solid), kinetic (dot-dashed), and thermal (dashed) energy of the gas particles inside the virial radius of the host halo, up to the point at which the central gas density reaches $n_{\rm H} = 10^4\,{\rm cm}^{-3}$ (top panels). The horizontal axis shows the time elapsed since the SN explosion. The bottom panels show the evolution of the baryon fraction computed within the central 30 pc (dashed) and within the virial radius (solid). The blue lines show the baryon fraction affected by both the SN and its progenitor, while the black lines represent the case when only the photoionization by the Pop III star is taken into account. The horizontal dotted lines show the universal baryon fraction.

A direct integration of Equation (1) then yields

$$c_i(t_0 + \Delta t) = c_i(t_0)e^{A\Delta t} + \frac{B}{A}(1 - e^{A\Delta t}), \qquad (5)$$

where $A = \sum_j K_{ij}$ and $B = \sum_j K_{ij}c_j$. We use Equation (5) to advance the concentrations of SPH active particles. In evaluating the right hand side, the densities and smoothing lengths are evaluated at the advanced time $t_0 + \Delta t$.

Initially, the metals from a SN are evenly distributed among the $\bar{N}_{\rm ngb}$ neighboring particles. Therefore, the initial metallicity of neighboring SPH particles is defined by

$$Z_i = \frac{m_{{\rm metal},i}}{m_{\rm SPH} + m_{{\rm metal},i}}, \qquad (6)$$

where the metal mass of individual SPH particles is $m_{{\rm metal,i}} = yM_*/\bar{N}_{\rm ngb}$, where y is the metal yield as given in Table 1.

3   RESULTS

In this section, we present our results. First, in Section 3.1, we show how the initial configuration for the SN explosion is affected by photoionization by the Pop III progenitor star as a function of the star's mass, and how it is affected by the environment provided by the host halo. In Section 3.2, we describe the evolution of the SN blast wave. In Section 3.3, we quantify the Pop III star's destructive impact in terms of the time scale on which baryons return to the center of the halo after the SN explosion, establishing conditions for the formation of a second generation of stars. In addition,

we also assess the properties of this second generation event, in particular the metallicity of the star-forming gas.

3.1   Photoionization

In our simulation box, the first star forms at $z \approx 28$ out of primordial gas inside a $M_{\rm vir} \approx 5 \times 10^5\,M_\odot$ minihalo. Fig. 2 shows the projected densities and temperatures of the gas surrounding the Pop III stars with masses $15\,M_\odot$, $25\,M_\odot$, and $40\,M_\odot$ (from left to right). The sizes and shapes of the H II regions, as depicted in Fig. 2, reflect the detailed transport of the ionizing photons emitted by the stars in the inhomogeneous density field of a given halo. Some gas around the $25\,M_\odot$ and $40\,M_\odot$ stars is photoheated to temperatures $\sim 10^4$ K, forming an extended H II region, whereas the ionized region created around the $15\,M_\odot$ star remains trapped inside the hydrodynamic shock, giving rise to a D-type ionization front. In the latter case, the time for ionizing photons to break out of the shock front, $t_{\rm B}$, is longer than the stellar lifetime, $t_{\rm B} > t_*$. Our results are consistent with those in Alvarez et al. (2006) and Whalen et al. (2008), where the authors find that no ionizing radiation will escape into the IGM for $M_* < 15\,M_\odot$. Specifically, in our simulations, the breakout times are 3.5 Myr and 1.95 Myr for the $25\,M_\odot$ and $40\,M_\odot$ stars (in HALO1).

The high ionizing luminosities of very massive Pop III stars with $M_* \gtrsim 100\,M_\odot$ are sufficient to photoevaporate even the densest gas in the halo, producing a smooth H II region (e.g., Greif et al. 2009; Jeon et al. 2012). On the other hand, as also noted by Abel et al. (2007), Bland-Hawthorn et al. (2011), and Ritter et al. (2012), at lower ionizing luminosities (say, from Pop III stars in the mass
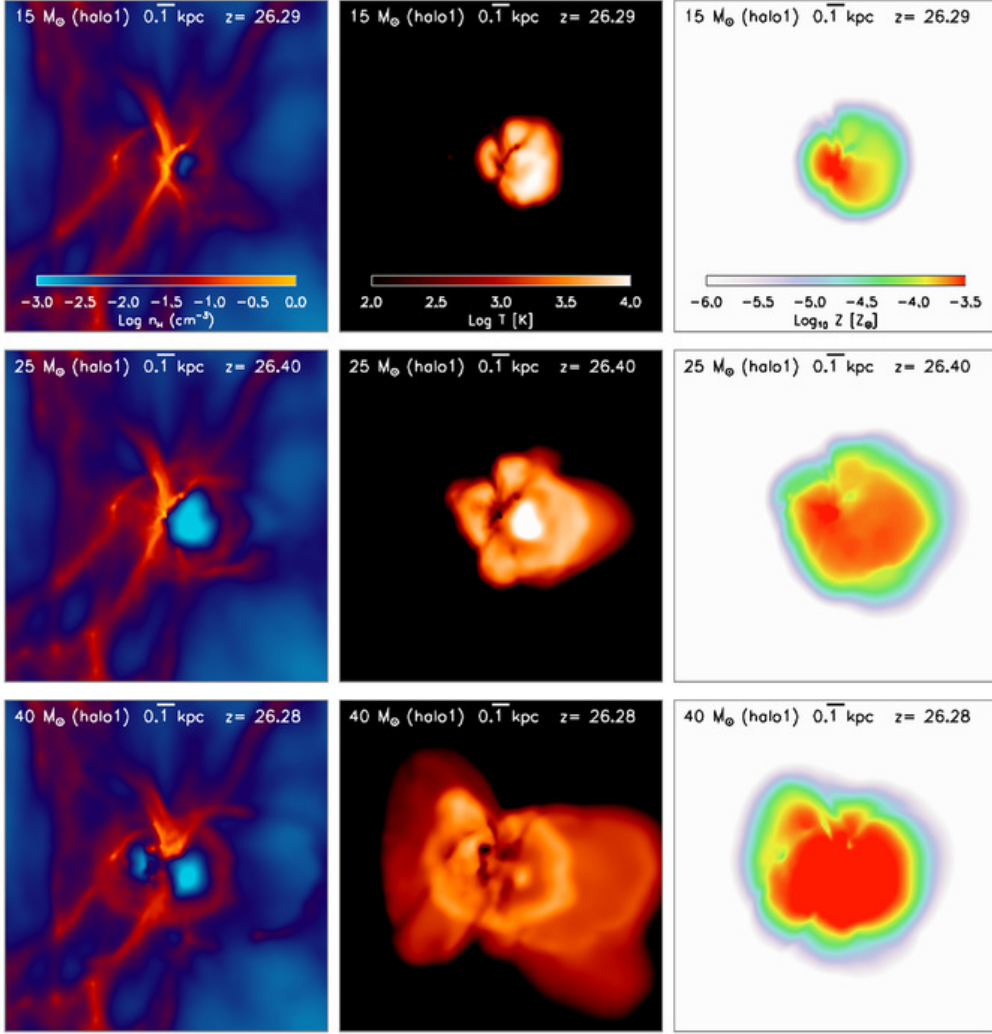
Figure 5. Projected hydrogen number densities (left), temperatures (middle), and metallicities (right) in the same slab as in Fig. 2 for Pop III progenitor star masses $15\,M_\odot$, $25\,M_\odot$, and $40\,M_\odot$, respectively (from top to bottom). The snapshots show the time at which the gas blown out by photoionization and the SN blastwave begins to flow back into the minihalo. This corresponds to $\approx 5\,\mathrm{Myr}$, $\approx 9\,\mathrm{Myr}$, and $\approx 15\,\mathrm{Myr}$ after the SN explosion for the $15\,M_\odot$, $25\,M_\odot$, and $40\,M_\odot$ stars, respectively. We emphasize that the simulations are identical except for the progenitor's ionizing luminosities, hence any differences in the results are entirely due to the sensitivity of the dynamics of the SN heated and accelerated gas to the pre-processing by ionizing radiation from the progenitor.

range $10\,M_\odot \lesssim M_* \lesssim 40\,M_\odot$), the densest clouds in the halo, often aligned with the filaments of the cosmic web, may self-shield and remain intact. The resistance to photoevaporation at low ionizing luminosities is also expected from analytical considerations (Bertoldi & McKee 1990). The residual neutral clouds cast shadows inside the halo and produce a highly asymmetrical, sometimes butterfly-shaped H II region.

These asymmetric structures are evident in Fig. 3 in the form of two distinct branches in the density and temperature radial profiles. Except for the $15\,M_\odot$ star, there are photo-heated gas particles with $n_{\mathrm{H}} \lesssim 1\,\mathrm{cm}^{-3}$ and $T \approx 10^4\,\mathrm{K}$ near the star, while at the same time, the gas embedded in a neighboring cosmic filament remains dense ($n_{\mathrm{H}} \gtrsim 100\,\mathrm{cm}^{-3}$) and cold ($T \sim 200\,\mathrm{K}$). The sizes of the H II regions are $\approx 800\,\mathrm{pc}$ and $\approx 1\,\mathrm{kpc}$ in diameter for the $25\,M_\odot$ and $40\,M_\odot$ stars, respectively (in HALO1). We note that even for a fixed Pop III stellar mass, the size of the resulting H II region could vary by a factor of 2, depending on halo environment.

For instance, the H II regions of a $40\,M_\odot$ Pop III star in HALO2 and HALO3 reach $\approx 1.8\,\mathrm{kpc}$ and $\approx 2\,\mathrm{kpc}$, respectively.

3.2 Supernova blastwaves

The SN is triggered at the end of the progenitor's lifetime, when the preceding photoionization has significantly modified the conditions in the ambient gas. Thus, the explosions occur in a wide range of environments, as discussed in Section 3.1. In most simulations, we choose an explosion energy of $E_{\mathrm{SN}} = 10^{51}$ ergs. We also perform an additional run for the $40\,M_\odot$ star (in HALO1) with $E_{\mathrm{SN}} = 6 \times 10^{50}$ ergs. Due to the limited resolution, the explosions are initiated after the end of the free expansion phase, where the ejecta mass roughly equals the swept-up mass. The time when the free expansion phase ends (Kitayama & Yoshida 2005)

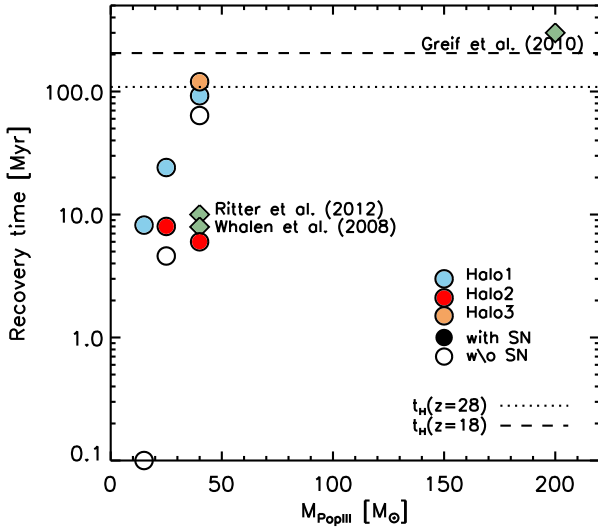$$t_{\mathrm{fe}} = 1.6 \times 10^4\,\mathrm{yr}$$

Figure 6. Recovery times for the central gas disturbed by photoionization and the SN blastwave as a function of Pop III progenitor mass. Colors are used to distinguish between haloes. The recovery times from simulations of stars in HALO1 with an H II region but no SN in which gas outflow was driven solely by the radiation-hydrodynamical response to photoionization heating, are marked by open circles. For comparison, results from previous studies are shown by diamonds.

$$\times \quad \left(\frac{n_{\rm H}}{1 \ {\rm cm}^{-3}}\right)^{-1/3} \left(\frac{M_{\rm ej}}{200 \, M_\odot}\right)^{5/6} \left(\frac{E_{\rm SN}}{10^{51} \ {\rm ergs}}\right)^{-1/2} \quad (7)$$

is $\approx 200 \, {\rm yr}$, $\approx 2.8 \times 10^3 \, {\rm yr}$, and $\approx 4.7 \times 10^3 \, {\rm yr}$ for the $15 \, M_\odot$, $25 \, M_\odot$ and $40 \, M_\odot$ stars, respectively. The latter two expand freely on time scale $t_{\rm fe}$ comparable to the time step, $\Delta t \approx 10^3 - 10^4 \, {\rm yr}$, encountered in our simulations. The injection of the SN energy leads to a sudden increase in the mean temperature of the particles near the explosion to $T_{\rm init} \approx 5 \times 10^7 \, {\rm K}$.

Subsequently, the thermal SN energy is rapidly converted into kinetic energy (see the top panels of Fig. 4), at $\approx 2-3\times10^{-3}$ Myr for the $15 \, M_\odot$ and $25 \, M_\odot$ cases, and at ≈ 0.1 Myr for the $40 \, M_\odot$ case. As the resulting blast wave propagates outward, the gas cools by adiabatic expansion. Afterwards, forming a dense shell, the energy of the gas behind the shock is radiatively lost primarily via inverse Compton scattering against the CMB, and also by free-free emission. In particular for the $15 \, M_\odot$ and $25 \, M_\odot$ stars, due to the initial configuration where the density of nearby gas remains high ($n_{\rm H} \gtrsim 10^3 \, {\rm cm}^{-3}$), the free-free cooling, operating on a timescale, $t_{\rm cool,ff} \propto 1/n_{\rm H}$, plays an important role in decreasing temperatures to $10^6 \, {\rm K}$ within < 0.5 Myr. Once the gas cools to $\sim 10^6 \, {\rm K}$, H and He resonance processes begin to dominate the cooling. As the blastwave energy dissipates, it eventually drops below the total binding energy of the gas, $E_{\rm B} = 3GM_{\rm vir}M_{\rm b}/(5R_{\rm vir})$, where $M_{\rm b} \simeq \Omega_{\rm b}/\Omega_{\rm m} \times M_{\rm vir}$ is the total baryonic mass, and $M_{\rm vir}$ and $R_{\rm vir}$ are the virial mass and radius of the given halo, respectively.

In Fig. 4 (bottom panels), we illustrate the evolution of the baryon fraction, both within the virial radius of the host halo and within the central 30 pc from the SN explosion site, up to the point when the central gas becomes dense enough to support new star formation. For comparison, we also show the evolution of the baryon fraction when only photoionization by the Pop III star was enabled, with no subsequent SN explosion (denoted by the black lines in Fig. 4). Fig. 4 shows that photoionization by the $40 \, M_\odot$ Pop III star was already strong enough to blow out most of the gas, at

$r \lesssim 30 \, {\rm pc}$, resulting in a significant decrease of the baryon fraction to $f_{\rm b} \approx 0.01$ prior to the SN explosion. At 9 Myr after the death of the star, about 80% of the gas mass is driven out of the virial radius. The resulting deficit of gas at the center lasts for 42 Myr and 3.5 Myr with and without SN explosion, respectively. The relative impact of the SN explosion on the central region is stronger in the $25 \, M_\odot$ case. This can be seen by comparing the baryon fraction with and without SN explosion, the latter remaining nearly constant over the run time, and dropping by 40% at ≈ 9 Myr when the SN is included. After ≈ 8 Myr, ≈ 9 Myr, and ≈ 50 Myr for the $15 \, M_\odot$, $25 \, M_\odot$, and $40 \, M_\odot$ stars (in HALO1), the central baryon fraction starts to increase as the gravitational force pulls back the gas. The haloes then attain central densities of up to $n_{\rm H} = 10^4 \, {\rm cm}^{-3}$ within the next 2 Myr, 14 Myr, and 40 Myr, respectively.

In Fig. 5, we present the projected hydrogen number densities, temperatures, and metallicities for the $15 \, M_\odot$, $25 \, M_\odot$, and $40 \, M_\odot$ stars (from top to bottom). The snapshots show the time at which the gas flow reverses from net outflow to inflow. After 1 Myr, for the $40 \, M_\odot$ star, the forward shock passes $r_{\rm sh} \approx 120$ pc, beyond the virial radius of the host halo, $R_{\rm vir} \approx 75$ pc. As the shock propagates, the central gas densities decrease over 1 Myr from $n_{\rm H} \approx 0.8 - 1 \, {\rm cm}^{-3}$ to $n_{\rm H} \approx 0.01 \, {\rm cm}^{-3}$ for the $25 \, M_\odot$ and $40 \, M_\odot$ stars, and from $n_{\rm H} \approx 10^4 \, {\rm cm}^{-3}$ to a few $n_{\rm H} \approx 10^3 \, {\rm cm}^{-3}$ for the $15 \, M_\odot$ star. Similar to the expansion direction of the H II region, the SN energy is preferentially transferred into underdense regions, perpendicular to the direction of cosmic filaments.

3.3 Onset of second generation star formation

3.3.1 Recovery timescale

We next estimate the recovery timescale, defined as the time delay between the first star formation event in a given halo and the recollapse of the gas affected by photoionization and the SN blastwave to high densities, such that a second generation of stars can form. This timescale sensitively depends on the SN progenitor mass. If we consider the same SN input energy, the difference in recovery timescale arises solely from the pre-explosion configuration shaped by the stellar-mass-dependent ionizing luminosity. Specifically, more massive Pop III stars have a stronger impact on the ambient gas, suppressing central gas densities prior to the explosion more strongly. As a consequence, the SN remnants suffer smaller radiative losses, and are thus able to escape further into the IGM. In our simulations, we find recovery times of ≈ 8 Myr, ≈ 24 Myr, and ≈ 90 Myr for the $15 \, M_\odot$, $25 \, M_\odot$, and $40 \, M_\odot$ stars, respectively (in HALO1). These timescales are shorter by 8 Myr, 15 Myr, and 30 Myr when no SN explosion is included (see open circles in Fig. 6).

In Fig. 6 we also mark the results from Greif et al. (2010), where they followed the evolution of the gas after a $200 \, M_\odot$ PISN explosion. Given that we here use the same initial conditions as in Greif et al. (2010), a direct comparison is possible. The recovery time in their work was of order the Hubble time, ≈ 300 Myr, at $z \approx 10$. On the other hand, the work by Ritter et al. (2012), where they studied the gas evolution and metal enrichment from a $40 \, M_\odot$ core collapse SN with $E_{\rm SN} = 10^{51}$ ergs, suggests a shorter recovery timescale, $\lesssim 10$ Myr. The reason for the much shorter recovery timescale compared to our simulation of a SN explosion with a $40 \, M_\odot$ progenitor, is twofold. First, their halo mass at recovery was $2 \times 10^6 \, M_\odot$, which is four times higher than the mass of our HALO1. Second, as they explain in their Section 2.4, their treatment of the pre-explosion photoionization by the Pop III progenitor artif-
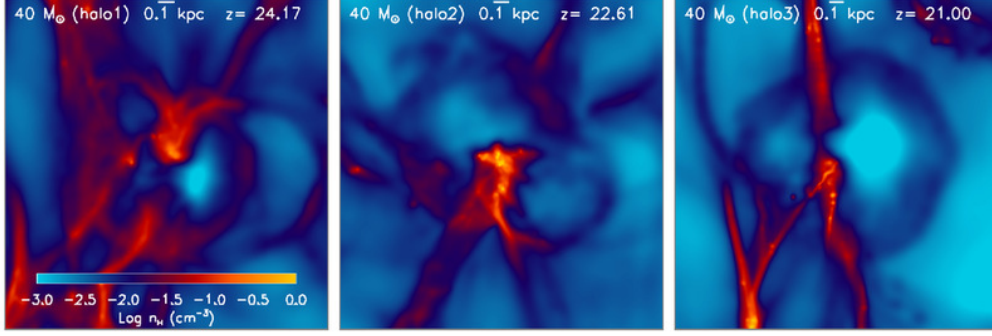
Figure 7. Hydrogen number densities 25 Myr after the SN explosion for the $40\,M_\odot$ progenitor in different environments. The central gas in HALO2 (middle) has already recovered to form a second generation of stars, while that in HALO1 (left) and HALO3 (right), which are less massive, still shows low central densities.

ically underestimated the degree of photoheating, such that gas densities remained high. Any radiative losses from the SN blastwave thus were overestimated. In addition to the core-collapse SNe, we show the case of a $40\,M_\odot$ hypernova with an energy 3×10^{52} ergs exploding in a substantially more massive halo of $1.2 \times 10^7\,M_\odot$ (Whalen et al. 2008). Here, the gas again quickly recollapses in ≈ 8 Myr. This broad range of recovery timescales suggests a strong dependence on environment.

To explore this environmental dependence, we have performed additional simulations by assuming that a $40\,M_\odot$ or a $25\,M_\odot$ Pop III star forms in HALO2 with mass $\approx 10^6\,M_\odot$ and HALO3 with mass $\approx 3 \times 10^5\,M_\odot$. We use the same explosion energy $E_{\rm SN} = 10^{51}$ erg in all cases. Due to the deeper potential well of HALO2, the deleterious impact of the Pop III stars is weaker than in HALO1 and HALO3. In HALO2, a larger fraction of the gas is more likely to resist photoevaporation by the $40\,M_\odot$ Pop III star, maintaining central densities of $n_{\rm H} \approx 10^4\,{\rm cm}^{-3}$. These are substantially higher than the typical densities in HALO1 when exposed to the same Pop III stellar radiation. Consequently, the SN remnants encounter higher density gas, thus experiencing more rapid energy dissipation through radiative cooling, leading to a shorter recovery time. Specifically, the estimated recovery time for the $40\,M_\odot$ star in HALO2 is ≈ 7 Myr, similar to the recovery time found in Ritter et al. (2012), which investigated a $40\,M_\odot$ Pop III star exploding in a halo with mass $\approx 10^6\,M_\odot$.

On the other hand, the impact of the Pop III feedback in HALO3 extends to much longer times: it takes more than 100 Myr for the gas expelled by photoionization and the SN blastwave of a $40\,M_\odot$ star to recollapse to high densities. This is largely due to the rather isolated environment of HALO3 which impedes gas accretion onto the halo. In Fig. 7, we compare the density field in different haloes 25 Myr after the SN explosion for the $40\,M_\odot$ case. In all haloes, the hydrodynamic shock driven by the explosion propagates to $\approx 400 - 600$ pc. While the central gas in HALO2 (middle panel of Fig. 7) has already reached densities high enough to fulfill the condition for star formation, densities in HALO1 and HALO3 are still low.

Next, we address the question of when the gas flow changes sign, reverting from net outflow to inflow. Fig. 8 presents the evolution of the gas (circles) and metal (triangles) flow through a sphere of radius 30 pc, centered on the location of the SN explosion. Inflow dominates after ≈ 6 Myr, ≈ 8 Myr, and ≈ 11 Myr after the SN for the $15\,M_\odot$, $25\,M_\odot$, and $40\,M_\odot$ stars (in HALO1). Along with the gas, metal-enriched material is brought back in. The transition
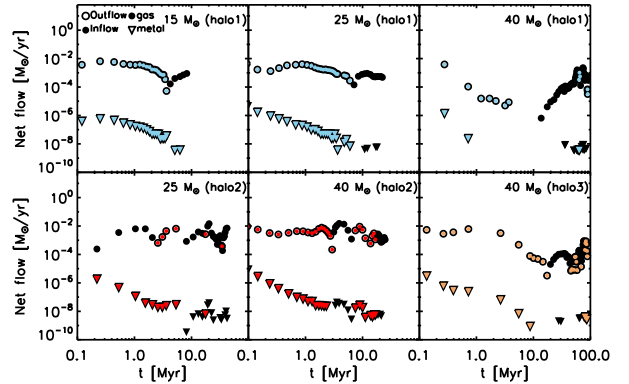
Figure 8. Gas (circles) and metal (upside down triangles) net mass flow rate through a sphere of radius 30 pc centered on the location of the SN explosion. Black and colored circles distinguish between inflow and outflow.

from net outflow to inflow for the metals occurs a few million years after it has occurred for the gas regardless of the metal content. The situation is more complicated in HALO2. For the $40\,M_\odot$ case, the transition happens at ≈ 3 Myr, but again reverting into an outflow for the next 25 Myr. This unstable flow is due to the environmental complexity, leading to unsteady accretion. We also note that the stellar feedback from the $25\,M_\odot$ Pop III star in HALO2 is initially not strong enough to reverse the cosmological inflow of gas, resulting in a delayed outflow until ≈ 2 Myr after the SN explosion.

3.3.2 Metallicity of star-forming gas

To what levels can the first SNe, triggered by Pop III stars, enrich the surrounding medium prior to the onset of second generation star formation? For the $40\,M_\odot$ star, the total mass in heavy elements, $yM_* \simeq 2\,M_\odot$, is initially distributed evenly among $\bar{N}_{\rm ngb} = 32$ nearby SPH particles, resulting in a metallicity of $yM_*/(m_{\rm SPH}\bar{N}_{\rm ngb}) = 0.0125$. Afterwards, metal dispersal is modeled as a diffusion process, as described in Section 2.4. As seen in the top panels of Fig. 9, at the end of the simulation the metals from the $15\,M_\odot$ case can penetrate to $r \approx 600$ pc, mainly enriching the underdense regions ($n_{\rm H} \approx 0.01$) to $\sim 5 \times 10^{-4}\,Z_\odot$, while the high density regions are kept primordial. About 17%, 20%, and 42% of the gas mass within 600 pc is enriched above $10^{-4}\,Z_\odot$ for
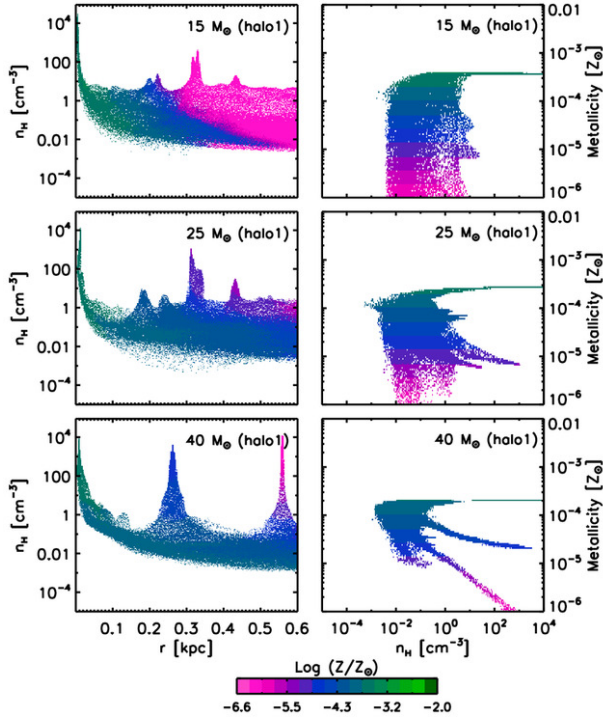
Figure 9. Hydrogen number density as a function of distance from the SN (left) and the metallicity as a function of the hydrogen number density (right) for the 15, 25, and 40 $M_\odot$ Pop III star (from top to bottom), all shown at the corresponding recovery times.

the 15 $M_\odot$, 25 $M_\odot$, and 40 $M_\odot$ stars, respectively. The typical extent to which the metals are dispersed is ≈ 550 pc, ≈ 1 kpc, and ≈ 1.5 kpc, for the 15 $M_\odot$, 25 $M_\odot$, and 40 $M_\odot$ stars, respectively. As expected, metal dispersion preferentially proceeds into the low-density phases of the IGM.

Interestingly, in HALO1 the central gas at $r \lesssim 10$ pc, where densities are high enough to form stars, is enriched to $2 - 6 \times 10^{-4}$ $Z_\odot$. This is above the critical metallicity, $Z_{\rm crit} \simeq 10^{-3.5}$ $Z_\odot$, for enabling low-mass star formation via metal or dust grain cooling. As shown in the left-bottom panel of Fig. 9, there are other high density peaks close to $n_{\rm H} = 10^4$ cm^{-3} within the central 600 pc. The high density gas ($n_{\rm H} \gtrsim 100$ cm^{-3}) near $r = 560$ pc has not yet been contaminated with metals, while the surrounding, relatively low density gas, is enriched to $\gtrsim 10^{-5}$ $Z_\odot$. The high-density peak has avoided contamination because the gas collapsed into the halo prior to the arrival of the metals, and the mixing of metals into such pre-condensed structures was inefficient and slow. On the other hand, the density peak near $r \approx 260$ pc is enriched to $\gtrsim 10^{-5}$ $Z_\odot$, demonstrating the large range of possibilities.

Whether such levels of enrichment suffice to achieve the transition from primordial, high-mass dominated, star formation to a normal, low-mass dominated, (Pop II) mode, depends on the detailed physics behind $Z_{\rm crit}$. In elucidating this physics, significant uncertainties remain. By way of fine-structure line cooling, mainly involving C II and O I, metal-enriched gas is able to fragment to form low-mass ($M_* \lesssim 0.8$ $M_\odot$) Pop II stars (e.g., Bromm et al. 2001; Safranek-Shrader et al. 2014b; Safranek-Shrader et al. 2014a). For fine-structure cooling, the minimum metallicity required to enable widespread fragmentation, extending possibly to low-mass stars, is $Z_{\rm crit} \simeq 10^{-3.5}$ $Z_\odot$. A second pathway towards enabling low-mass star formation is through cooling by dust grains

produced during the first SNe explosions (e.g., Schneider et al. 2006). The critical metallicity in this scenario is a few orders of magnitude below that for the atomic line cooling scenario. Therefore, the density peak at ≈ 260 pc, enriched to a few 10^{-5} $Z_\odot$, is not capable of forming Pop II stars based on atomic line cooling alone, but it satisfies the condition for fragmentation set by dust cooling.

Do current observations, obtained by the stellar archeology of low-mass, metal-poor stars, provide us with hints for this theoretical debate? Most metal-poor stars with [Fe/H] < -4.0 found in the Hamburg/ESO survey (Frebel et al. 2006; Christlieb et al. 2008) satisfy the condition for fine-structure cooling (Frebel et al. 2007). In addition, the recently discovered star SMSS 0313-6708 has no detected iron, with an upper limit of [Fe/H] < -7.1, but exhibits a high carbon abundance, [C/H] $= -2.6$ (Keller et al. 2014), thus again exceeding the fine-structure threshold. However, there are counter-examples, specifically the most metal-poor star found to date, in which *all* elements, including C and O, are underabundant (Caffau et al. 2011). Here, dust cooling seems to be required. The empirical picture is thus complex, with possible roles for both cooling channels (Ji et al. 2014).

4 SUMMARY AND CONCLUSIONS

We have performed a suite of cosmological three-dimensional simulations to investigate the recovery from Pop III core-collapse SNe with a mass range for the progenitor stars of $M_* = 15 - 40$ $M_\odot$. We have also investigated the chemical impact of the SNe on the next episode of star formation.

We found that the radiative feedback from Pop III stars plays an important role in setting the initial configuration for the subsequent SN by reducing the gas density prior to the explosion. Unlike the photoionization by massive Pop III stars with $M_* \sim 100$ $M_\odot$, the radiative impact from less massive Pop III stars with $M_* \sim 15 - 40$ $M_\odot$ is less strong in evacuating gas out of the host halo. Therefore, the ejecta from the SNe are more likely to encounter a high density ambient medium, in which the ejecta cool more rapidly and may be re-accreted earlier. We find that the time it takes for the SN-processed gas to fall back into the halo that hosts a Pop III star with a moderate mass is of the order of a few 10 Myr. We also explore the effect of the environment by exploding SNe in different host haloes. We find that the impact of a Pop III SN explosion in a $M_{\rm vir} \sim 10^5$ $M_\odot$ halo is more violent than in a $M_{\rm vir} \sim 10^6$ $M_\odot$ halo.

In the context of hierarchical cosmology, structures assemble from the bottom up: smaller objects collapse first, making bigger structures. The first galaxies, thus, are believed to have grown by assembling roughly ~ 10 Pop III star-forming minihaloes (Fig. 10 and Greif et al. 2008). Theoretically, one often defines the first galaxies as the DM haloes with masses $M_{\rm vir} \sim 10^8$ $M_\odot$, collapsing at $z \simeq 10$. These objects are massive enough to retain the gas that was affected by previous star formation, and this gas inside the galaxy is able to cool via atomic hydrogen line emission. Previous works by, e.g., Wise & Abel (2008) and Greif et al. (2010) show that a single PISN explosion in a minihalo can be sufficiently violent, destroying the minihalo in which the PISN explodes and enriching the central star-forming gas in the nascent galaxy to 10^{-3} $Z_\odot$.

On the other hand, as shown in this work, the impact of core-collapse SNe with progenitor masses $15 - 40$ $M_\odot$ on the delay of gas collapse and thus on the next episode of star forma-
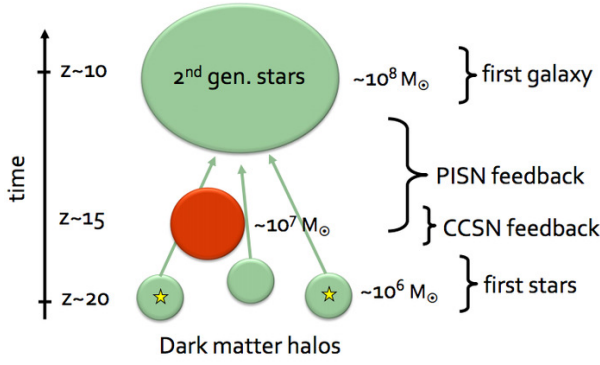
Figure 10. Assembly of a first galaxy under Pop III feedback. Minihaloes that host Pop III stars first collapse at $z \gtrsim 30$ and then grow for $\sim 300\,\mathrm{Myr}$ to assemble an atomically cooling galaxy in a $10^8\,M_\odot$ DM halo. The impact of a PISN is very destructive, delaying the gas collapse in the halo for $t_{\mathrm{recover}} \sim 300\,\mathrm{Myr}$ (Greif et al. 2010). On the other hand, the delay of second generation star formation that is introduced by Pop III core-collapse SNe is shorter, of the order of a few $10\,\mathrm{Myr}$. The properties of the first stars, in particular their mass, thus govern the nature of the first galaxies.

tion is prompt, $t_{\mathrm{recover}} \approx 10\,\mathrm{Myr}$. Depending on the halo environment and halo mass, this timescale may vary from $10\,\mathrm{Myr}$ to $100\,\mathrm{Myr}$, but always remains substantially smaller than the delay of $t_{\mathrm{recover}} \sim 300\,\mathrm{Myr}$ resulting from a PISN. This suggests that multiple star formation episodes, likely occurring in the Pop II mode, may be triggered at the site that was affected by core-collapse Pop III stars, even before the system evolves into a substantially more massive galaxy (e.g., Wise et al. 2012; Pawlik, Milosavljević, & Bromm 2013).

In summary, our simulations imply that the central cold and dense gas can be enriched above $Z = 10^{-4}\,\mathrm{Z_\odot}$ by a single core-collapse Pop III SN. Given the expected multiple star formation events before the collapse of the minihalo host into a $10^8\,M_\odot$ atomically cooling halo, it is likely that the central star-forming gas in the first galaxies is substantially polluted with metals, possibly initiating Pop II star formation in the first galaxies.

REFERENCES

Abel T., Bryan G. L., Norman M. L., 2002, Science, 295, 93
Abel T., Wise J. H., Bryan G. L., 2007, ApJ, 659, L87
Alvarez M. A., Bromm V., Shapiro P. R., 2006, ApJ, 639, 621
Alvarez M. A., Wise J. H., Abel T., 2009, ApJ, 701, L133
Barkana R., 2009, MNRAS, 397, 1454
Barkana R., Loeb A., 2001, Physics Reports, 349, 125
Bate M. R., Burkert A., 1997, MNRAS, 288, 1060
Bertoldi F., McKee C. F., 1990, ApJ, 354, 529
Bland-Hawthorn J., Sutherland R., Karlsson T., 2011, in Koleva M., Prugniel P., Vauglin I., eds, EAS Publications Series Vol. 48 of EAS Publications Series, The Minimum Mass for a Dwarf Galaxy. pp 397–404
Bromm V., 2013, Reports on Progress in Physics, 76, 112901
Bromm V., Coppi P. S., Larson R. B., 2002, ApJ, 564, 23
Bromm V., Ferrara A., Coppi P. S., Larson R. B., 2001, MNRAS, 328, 969
Bromm V., Larson R. B., 2004, ARA&A, 42, 79
Bromm V., Loeb A., 2003, Nature, 425, 812
Bromm V., Yoshida N., 2011, ARA&A, 49, 373
Bromm V., Yoshida N., Hernquist L., 2003, ApJ, 596, L135
Bromm V., Yoshida N., Hernquist L., McKee C. F., 2009, Nature, 459, 49
Caffau E., Bonifacio P., François P., Sbordone L., Monaco L., Spite M., Spite F., Ludwig H.-G., Cayrel R., Zaggia S., Hammer F., Randich S., Molaro P., Hill V., 2011, Nature, 477, 67
Chatzopoulos E., Wheeler J. C., 2012, ApJ, 748, 42
Christlieb N., Schörck T., Frebel A., Beers T. C., Wisotzki L., Reimers D., 2008, A&A, 484, 721
Ciardi B., Ferrara A., 2005, Space Sci. Rev., 116, 625
Clark P. C., Glover S. C. O., Klessen R. S., Bromm V., 2011, ApJ, 727, 110
Cooke R., Madau P., 2014, arXiv:1405.7369
Dopcke G., Glover S. C. O., Clark P. C., Klessen R. S., 2013, ApJ, 766, 103
Durier F., Dalla Vecchia C., 2012, MNRAS, 419, 465
Frebel A., Christlieb N., Norris J. E., Beers T. C., Bessell M. S., Rhee J., Fechner C., Marsteller B., Rossi S., Thom C., Wisotzki L., Reimers D., 2006, ApJ, 652, 1585
Frebel A., Johnson J. L., Bromm V., 2007, MNRAS, 380, L40
Glover S. C. O., Brand P. W. J. L., 2003, MNRAS, 340, 210
Greif T. H., Bromm V., Clark P. C., Glover S. C. O., Smith R. J., Klessen R. S., Yoshida N., Springel V., 2012, MNRAS, 424, 399
Greif T. H., Glover S. C. O., Bromm V., Klessen R. S., 2009, MNRAS, 392, 1381
Greif T. H., Glover S. C. O., Bromm V., Klessen R. S., 2010, ApJ, 716, 510
Greif T. H., Johnson J. L., Bromm V., Klessen R. S., 2007, ApJ, 670, 1
Greif T. H., Johnson J. L., Klessen R. S., Bromm V., 2008, MNRAS, 387, 1021
Greif T. H., Johnson J. L., Klessen R. S., Bromm V., 2009, MNRAS, 399, 639
Greif T. H., Springel V., White S. D. M., Glover S. C. O., Clark P. C., Smith R. J., Klessen R. S., Bromm V., 2011, ApJ, 737, 75
Haiman Z., Thoul A. A., Loeb A., 1996, ApJ, 464, 523
Heger A., Fryer C. L., Woosley S. E., Langer N., Hartmann D. H., 2003, ApJ, 591, 288
Heger A., Woosley S. E., 2002, ApJ, 567, 532
Heger A., Woosley S. E., 2010, ApJ, 724, 341
Hirano S., Hosokawa T., Yoshida N., Umeda H., Omukai K., Chiaki G., Yorke H. W., 2014, ApJ, 781, 60
Hosokawa T., Omukai K., Yoshida N., Yorke H. W., 2011, Science, 334, 1250
Jeon M., Pawlik A. H., Bromm V., Milosavljević M., 2014, MNRAS, 440, 3778
Jeon M., Pawlik A. H., Greif T. H., Glover S. C. O., Bromm V., Milosavljević M., Klessen R. S., 2012, ApJ, 754, 34
Ji A. P., Frebel A., Bromm V., 2014, ApJ, 782, 95
Joggerst C. C., Almgren A., Bell J., Heger A., Whalen D.,

Woosley S. E., 2010, ApJ, 709, 11

Johnson J. L., Greif T. H., Bromm V., Klessen R. S., Ippolito J., 2009, MNRAS, 399, 37

Karlsson T., Bromm V., Bland-Hawthorn J., 2013, Rev. Mod. Phys., 85, 809

Keller S. C., Bessell M. S., Frebel A., Casey A. R., Asplund M., Jacobson H. R., Lind K., Norris J. E., Yong D., Heger A., Magic Z., da Costa G. S., Schmidt B. P., Tisserand P., 2014, Nature, 506, 463

Kitayama T., Yoshida N., 2005, ApJ, 630, 675

Klessen R. S., Lin D. N., 2003, Physical Review E, 67, 046311

Kuhlen M., Madau P., 2005, MNRAS, 363, 1069

Loeb A., Furlanetto S. R., 2013, The First Galaxies in the Universe

Maeder A., Meynet G., 2012, Rev. Mod. Phys., 84, 25

Maio U., Ciardi B., Dolag K., Tornatore L., Khochfar S., 2010, MNRAS, 407, 1003

Milosavljević M., Bromm V., Couch S. M., Oh S. P., 2009a, ApJ, 698, 766

Milosavljević M., Couch S. M., Bromm V., 2009b, ApJ, 696, L146

Omukai K., 2000, ApJ, 534, 809

Park K., Ricotti M., 2011, ApJ, 739, 2

Pawlik A. H., Schaye J., 2008, MNRAS, 389, 651

Pawlik A. H., Schaye J., 2011, MNRAS, 412, 1943

Pawlik A. H., Milosavljević M., Bromm V., 2011, ApJ, 731, 54

Pawlik A. H., Milosavljević M., Bromm V., 2013, ApJ, 767, 59

Prieto J., Padoan P., Jimenez R., Infante L., 2011, ApJ, 731, L38

Raičević M., Pawlik A. H., Schaye J., Rahmati A., 2014, MNRAS, 437, 2816

Ritter J. S., Safranek-Shrader C., Gnat O., Milosavljević M., Bromm V., 2012, ApJ, 761, 56

Robertson B. E., Ellis R. S., Dunlop J. S., McLure R. J., Stark D. P., 2010, Nature, 468, 49

Safranek-Shrader C., Milosavljević M., Bromm V., 2014a, MNRAS, 440, L76

Safranek-Shrader C., Milosavljević M., Bromm V., 2014b, MNRAS, 438, 1669

Saitoh T. R., Makino J., 2009, ApJ, 697, L99

Schaerer D., 2002, A&A, 382, 28

Schaerer D., 2003, A&A, 397, 527

Schaye J., Dalla Vecchia C., Booth C. M., Wiersma R. P. C., Theuns T., Haas M. R., Bertone S., Duffy A. R., McCarthy I. G., van de Voort F., 2010, MNRAS, 402, 1536

Schmidt W., Federrath C., 2011, A&A, 528, A106

Schmidt W., Niemeyer J. C., Hillebrandt W., 2006, A&A, 450, 265

Schneider R., Ferrara A., Natarajan P., Omukai K., 2002, ApJ, 571, 30

Schneider R., Omukai K., Inoue A. K., Ferrara A., 2006, MNRAS, 369, 1437

Shu F. H., 1992, The physics of astrophysics. Volume II: Gas dynamics, University Science Books, Mill Valley, CA (USA)

Smith R. J., Glover S. C. O., Clark P. C., Greif T., Klessen R. S., 2011, MNRAS, 414, 3633

Springel V., 2005, MNRAS, 364, 1105

Springel V., White S. D. M., Tormen G., Kauffmann G., 2001, MNRAS, 328, 726

Stacy A., Greif T. H., Bromm V., 2010, MNRAS, 403, 45

Stacy A., Greif T. H., Bromm V., 2012, MNRAS, 422, 290

Stacy A., Bromm V., 2013, MNRAS, 433, 1094

Tegmark M., Silk J., Rees M. J., Blanchard A., Abel T., Palla F., 1997, ApJ, 474, 1

Turk M. J., Abel T., O'Shea B., 2009, Science, 325, 601

Umeda H., Nomoto K., 2005, ApJ, 619, 427

Venkatesan A., Benson A., 2011, MNRAS, 417, 2264

Whalen D., van Veelen B., O'Shea B. W., Norman M. L., 2008, ApJ, 682, 49

Wheeler J. C., Johnson V., 2011, ApJ, 738, 163

White S. D. M., 1996, in Schaeffer R., Silk J., Spiro M., & Zinn-Justin J. ed., Cosmology and Large Scale Structure Formation and Evolution of Galaxies.. p. 349

Wiklind T., Mobasher B., Bromm V., eds, 2013, The First Galaxies Vol. 396 of Astrophysics and Space Science Library

Wise J. H., Abel T., 2008, ApJ, 685, 40

Wise J. H., Turk M. J., Norman M. L., Abel T., 2012, ApJ, 745, 50

Yoon S.-C., Dierks A., Langer N., 2012, A&A, 542, A113

Yoshida N., Abel T., Hernquist L., Sugiyama N., 2003, ApJ, 592, 645

Yoshida N., Omukai K., Hernquist L., Abel T., 2006, ApJ, 652, 6

Zackrisson E., Rydberg C.-E., Schaerer D., Östlin G., Tuli M., 2011, ApJ, 740, 13